communications earth & environment

Article

A Nature Portfolio journal

https://doi.org/10.1038/s43247-025-02354-6

Divergent responses of historic rain-on-snow flood extremes to a warmer climate

Dalei Hao [1] ✉, Gautam Bisht[1], Donghui Xu [1], Mukesh Kumar [2] & L. Ruby Leung [1]

Global warming is altering flood risks induced by rain-on-snow events. However, decision-makers lack guidance on how rain-on-snow induced extreme floods could be altered with warming. Here, storyline analyses using a kilometer-scale land surface model reveal diverse responses of four historically-impactful, decision-relevant rain-on-snow induced extreme flood events over the contiguous U.S. to warming, due to alterations in their water budgets. For the 2017-Feb California floods, runoff first increases and then decreases with warming, peaking under the +3 K scenario, while runoff of the 2017-Jan California floods increases monotonically by ~53%/K. Contrastingly, runoff of the 1996-Jan Mid-Atlantic floods decreases gradually with warming. Despite these differences, warming generally shifts flood-generating regimes along elevation profiles. High elevations could experience notably increased runoff, while low elevations encounter a shift from rain-on-snow-driven to rainfall-dominated runoff. These findings underscore the need for flood control planning to quantify region- and elevation-specific changes in rain-on-snow events in a warmer climate.

Rain-on-snow (ROS) events occur when rain falls on a preexisting and ripened snowpack[1], and tend to induce high flood risks, due to the combined contributions from both rainfall and snowmelt[2,3]. Historically, several destructive extreme flood events have been triggered by ROS events with devastating societal and economic consequences over the contiguous United States (CONUS)[4,5]. Well-publicized examples include the 1996 Pacific Northwest floods (1996PacN), causing 8 deaths, a loss of about 500 million dollars in flood damages, and thousands of people evacuated[6], the 1996 January Mid-Atlantic floods (1996MidA), resulting in 30 fatalities and damages of ~$1.5 billion[7,8], and the 2017 California floods (including two events in January and February: 2017CA-Jan and 2017CA-Feb) which damaged the Oroville Dam and led to an emergency evacuation of around 190,000 people[9]. Other extremely severe and extensive floods induced by ROS over CONUS were identified and reported in ref. 10. Examining and understanding these catastrophic, ROS-induced extreme flood events are valuable for mitigating flood risks.

Global warming is projected to alter ROS event characteristics (e.g., severity, frequency, distribution, timing, and duration) and corresponding flood risks. A warmer air temperature can favor rainfall over snowfall[11,12], increase extreme precipitation[13,14], accelerate snowmelt[15,16], and reduce antecedent snowpack conditions, causing a notable decreasing trend of ROS and ROS-induced floods, especially over low-elevation regions of the western US in the past six decades[4,17]. The eastern US has shown region- and season-dependent increasing or decreasing trends of ROS in recent decades[18,19]. A warming future is projected to decrease the ROS frequency at lower elevations, but increase the ROS flood risks at higher elevations over CONUS[5,20]. Characterizing the large-scale trends and variations in ROS events and the associated flood risks under a warmer climate, previous studies have highlighted the need to update and upgrade regional infrastructure for future flood protection.

However, decision-makers and stakeholders still lack guidance on how ROS-induced extreme flood events with severe impacts would respond to a warmer climate. To develop warming-adapted mitigation strategies and increase resilience to unprecedented ROS-induced extreme floods (e.g., 1996PacN, 1996MidA, 2017CA-Jan, 2017CA-Feb), it is important to understand how these extreme events will evolve in the plausible future. The event-oriented storyline approach is well suited for this purpose, as it can be used to evaluate the climate risks of a historic extreme event under plausible narratives or contextual scenarios to gain actionable knowledge[21,22]. This approach conditions climate risk by reconstructing historically impactful and decision-relevant extreme events and explores their physical processes and plausible future[21,23,24]. The storyline approach has been used to determine the future risks of the 1996MidA event and reveal its sensitivity to warming at a spatial resolution of 14 km[25]. However, the coarse-scale storyline simulations cannot resolve ROS events' strong climate- and elevation-dependent sensitivity. High-resolution (e.g., kilometer-scale) simulations are necessary to accurately capture the climatic and topographic controls on precipitation magnitude, rain-snow phase separation, and the formation, persistence, and melt of snowpack during the ROS events[20]. Notably, the storyline approach was recently applied to analyze the

[1]Atmospheric, Climate, & Earth Sciences Division, Pacific Northwest National Laboratory, Richland, WA, USA. [2]Department of Civil, Construction, and Environmental Engineering, University of Alabama, Tuscaloosa, AL, USA. ✉e-mail: dalei.hao@pnnl.gov

California-Nevada New Year's flood event of 1997 using coupled atmosphere-land simulations that were regionally refined to 3.5 km over the study region of interest, providing insights on the sensitivity of the flood drivers to warming[26,27].

Despite the aforementioned studies, how different ROS-induced extreme flood events will respond to a warmer climate at the kilometer scale remains underexplored. Given that different ROS flood events exhibit distinct thermodynamic conditions and depend on geographic location and topographic characteristics, we hypothesize that extreme ROS flood events will show diverse and elevation-dependent responses in warmer climates. Thus, kilometer-scale storyline analysis focusing on multiple unprecedented extreme events is urgently needed to raise public awareness and strengthen decision-making for ROS-induced floods under global warming.

This study combines kilometer-scale land surface model simulations and storyline analysis to mechanistically understand how multiple historic ROS-induced extreme flood events respond to a warmer climate. First, considering their catastrophic impacts, we selected four ROS-induced extreme flood events (i.e., 1996PacN, 1996MidA, 2017CA-Jan, and 2017CA-Feb) over CONUS. These events have been widely studied by researchers[25,28–30], and used by government officials and flood emergency managers as a reference in operations[31]. Second, we performed 1 km hindcast simulations of the four events using the state-of-the-science Energy Exascale Earth System Model (E3SM) Land Model (ELM)[32]. ELM can mechanistically simulate frozen ground and its thawing and refreezing, which could play an important role in soil infiltration and runoff generation[33]. Model calibration and atmospheric forcing dataset selection were performed separately for each study region to accurately capture snowpack and runoff dynamics. Further, we used the calibrated ELM to perform five 1 km resolution delta-warming simulations for all selected ROS events. For the delta-warming simulations, we ran ELM simulations starting one year before the events with the warmer climate forcings to ensure initial conditions for the ROS events were consistent with the climate scenarios. These five warming simulations feature a spatially uniform air temperature increase from 1 K to 5 K with a 1 K increment. The +1 K and +5 K scenarios approximately correspond to the US warming projected at the end of the 21st century under the optimistic low-emission and the "business as usual" scenarios, respectively[34]. Associated with warming, we also imposed precipitation changes using a simple spatially uniform scaling of 7% per K of warming, as heavy precipitation typical of flood-causing ROS events generally increases due to the increase of atmospheric water vapor with temperature following the Clausius-Clapeyron relationship[35]. We used the 1 km hindcast and future simulations to uncover the sensitivity of snowpack and runoff to warming for the four events, in terms of the changes in magnitude, peak timing, spatial variations, and elevation profiles. We also quantified the altered water budgets to clarify the underlying mechanism of similar or divergent responses of different events to a warmer climate.

Results

Recreating the historic ROS extreme flood events

The four historic ROS extreme flood events over the three flood-prone basins with varying elevation distributions (Figs. 1 and S1) are all driven jointly by both heavy rainfall and rapid snowmelt (see Methods for details). For all four events, the 1 km ELM simulations with the default parameter values and driven by four different atmospheric forcing datasets (see

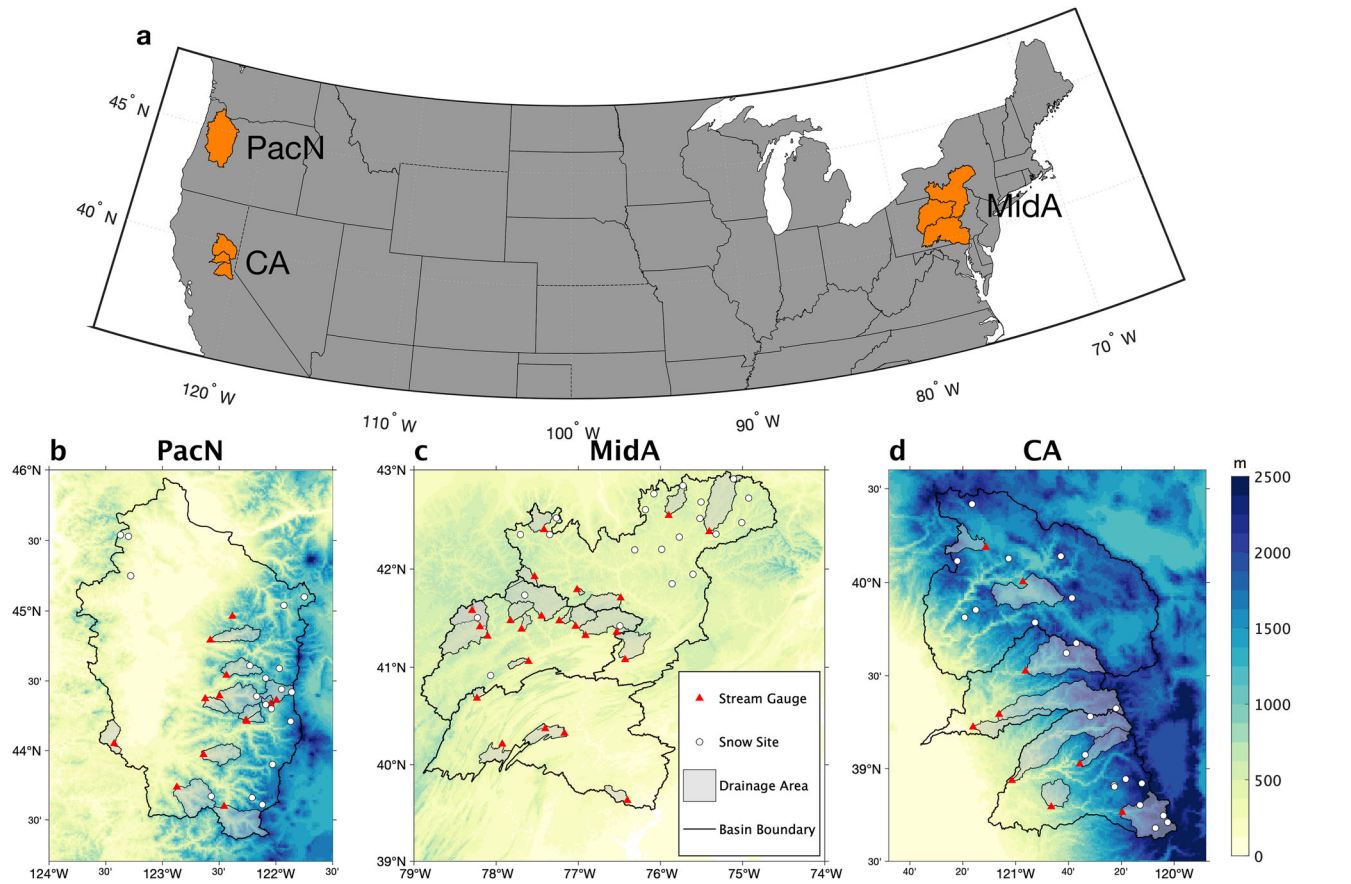

Fig. 1 | Geographic locations of the three study domains and the spatial distribution of surface elevation. a The geographic locations of three study domains in the Pacific Northwest (PacN) region, Mid-Atlantic (MidA) region, and California (CA), over the contiguous United States. **b** The Willamette basin. **c** The Susquehanna River Basin comprising of western, upper and lower parts. **d** The Feather, Yuba, and American River basins (from top to bottom). In (**b**–**d**), the basins are outlined by the black lines, the red triangles and white circles are the US Geological Survey (USGS) stream gauges and snow monitoring stations, and the gray shading represents the drainage area for each USGS stream gauge.

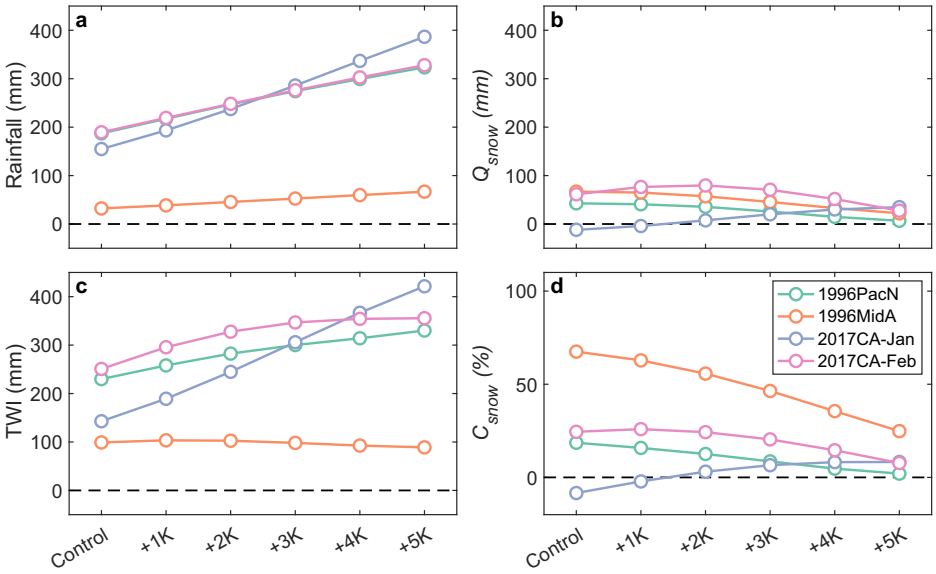

Fig. 2 | Warming-driven responses of basin average cumulative rainfall, sum of liquid water retention and snowmelt (Q_{snow}), terrestrial water input (TWI), and relative snow contribution to TWI (C_{snow}). a-d, Basin average rainfall, Q_{snow}, TWI, and C_{snow} under the Control and warming scenarios, for the four events: 1996PacN, 1996MidA, 2017CA-Jan, and 2017CA-Feb distinguished by the different colors.

Methods; Table S1) show varying performance in simulating daily snow water equivalent (SWE) when compared against the daily field measurements from the Snow Telemetry (SNOTEL) and the Northern Hemisphere Snow Water Equivalent (NH-SWE) data (see Methods; Fig. S2; Table S2), with the correlation coefficients (R) varying from 0.24 to 0.75. The daily simulated runoff shows R values ranging from 0.49 to 0.90 when compared to the benchmark dataset from the Global Reach-level Flood Reanalysis (GRFR) data[36] (see Methods; Fig. S2; Table S2). After determining the optimal atmospheric forcing dataset with the best performance separately for each event region, we further identified and calibrated the sensitive ELM parameters for snowpack and runoff simulations for each region (see Methods; Table S3). The region-specific optimal atmospheric forcings and calibrated snowpack- and runoff-related parameter settings are shown in Table S4. Both the atmospheric forcing selection and parameter calibration show considerable impacts on basin-wide runoff during the four ROS events (Table S5). Following these steps, the hindcast ELM simulations show improved performance in simulating snowpack and runoff on a daily scale with increased R values of ≥0.72 for SWE and ≥0.86 for runoff, as well as reduced biases (Table S2; Fig. S3), demonstrating that ELM can well reproduce the four extreme events.

The major ROS flood drivers, as well as the snow contribution, differ among the events in the ELM hindcast simulations. We defined the terrestrial water input (TWI) as the total liquid water input into the soil during the event, following ref. 2. TWI is mainly sourced from rainfall and snowmelt. However, the interaction between cold snowpack and rainfall could retain or refreeze the liquid rain within the snowpack[37], which means that TWI may be smaller than the rainfall. Thus, we used the sum of liquid water retention and snowmelt (Q_{snow}) to represent the total snow effects. We further defined the relative contribution of snow (C_{snow}) as the ratio of Q_{snow} to TWI. Note that Q_{snow} and C_{snow} can be negative when liquid water retention effects are stronger than the snowmelt effects. At the basin scale, due to the relatively higher rainfall than Q_{snow} (Fig. 2a, b), 1996PacN shows a C_{snow} value of 18.6% (Fig. 2d), which is slightly lower than the range of 21–57% at the SNOTEL stations reported by ref. 28. This difference is potentially because we focus on the entire Willamette basin, where the snow cover is lower in the western regions (Fig. S4). For 1996MidA, snow contribution accounts for about 67.5% of TWI, which is in line with the model estimates of ~70% in ref. 25. For 2017CA-Jan, rainfall dominates TWI, and C_{snow} is negative (−8.4%), potentially due to the relatively cold air temperature (Fig. S5) and deep snowpack over the high-elevation northeastern mountainous regions (Fig. S4) and thus strong effects of liquid water retention[37]. For 2017CA-Feb, C_{snow} is 24.5%, which is close to the estimated value of 25% from a previous study[30] over the Sierra Nevada. The elevation profiles (Fig. 3) and spatial patterns (Fig. S6) of C_{snow} for each event are modulated by the spatially-varying topography and snowpack characteristics. These results indicate that snowpack plays a different role in different regions and events, complicating the ROS flood forecasting and risk evaluation.

Changing ROS flood drivers under warming

The ROS flood drivers in different events respond to warming in different ways, due to the change of rainfall and Q_{snow} (Fig. 2a–c), as shown by the difference between the hindcast (Control) and the five delta-warming simulations (see Methods). As one of the main sources of TWI, rainfall in all four events shows an increasing trend with warming (Fig. 2a) due to the increase in extreme precipitation (see Methods), and more precipitation falling as rain rather than snow with increased air temperature[11,38]. However, Q_{snow} and TWI in different events show different responses to warming in magnitude and direction (Fig. 2b, c). TWI of 1996MidA first increases and reaches a maximum under the +1 K scenario, and then decreases with further warming. Despite the nonlinear response, the TWI change of 1996MidA under warming is relatively small. The other three events show a gradually increasing trend of TWI with warming. Among all the simulated events, 2017CA-Jan shows the largest increase with warming.

The TWI responses are jointly determined by the relative change of rainfall and Q_{snow} (Fig. 2). For all four events, the initial SWE decreases with warming due to increasing snowmelt before the event, which means the total available SWE for melting during the ROS event decreases in the future (Figure S7). Therefore, with warming, Q_{snow} and C_{snow} show an overall decreasing trend except for the monotonic increasing trend for 2017CA-Jan (Fig. 2d) due to the relatively cold air temperature over the snow regions (Figure S5). For 1996PacN and 2017CA-Feb, the rainfall increase dominates the TWI increase under warming despite the reduced Q_{snow}, while for 1996MidA, the Q_{snow} reduction is comparable to the rainfall increase (Fig. 2b, c). For 2017CA-Jan, the concurrent increase of rainfall and snowmelt causes the linearly increasing response of TWI to warming.

The change in ROS flood drivers with warming is elevation-dependent (Fig. 3). Overall, driven by increasing rainfall (Fig. 3e–h), TWI increases along the elevation profiles (Fig. 3m-p) except for 1996MidA. For all four events, Q_{snow} is reduced at low elevations and increased at high elevations (Fig. 3i–l), which further regulates the elevation-dependent responses of TWI to warming. For 1996PacN, high elevations show a larger increase of TWI with warming due to the combined positive contributions from rainfall and snowmelt (Fig. 3m). The elevation at which C_{snow} peaks increases with

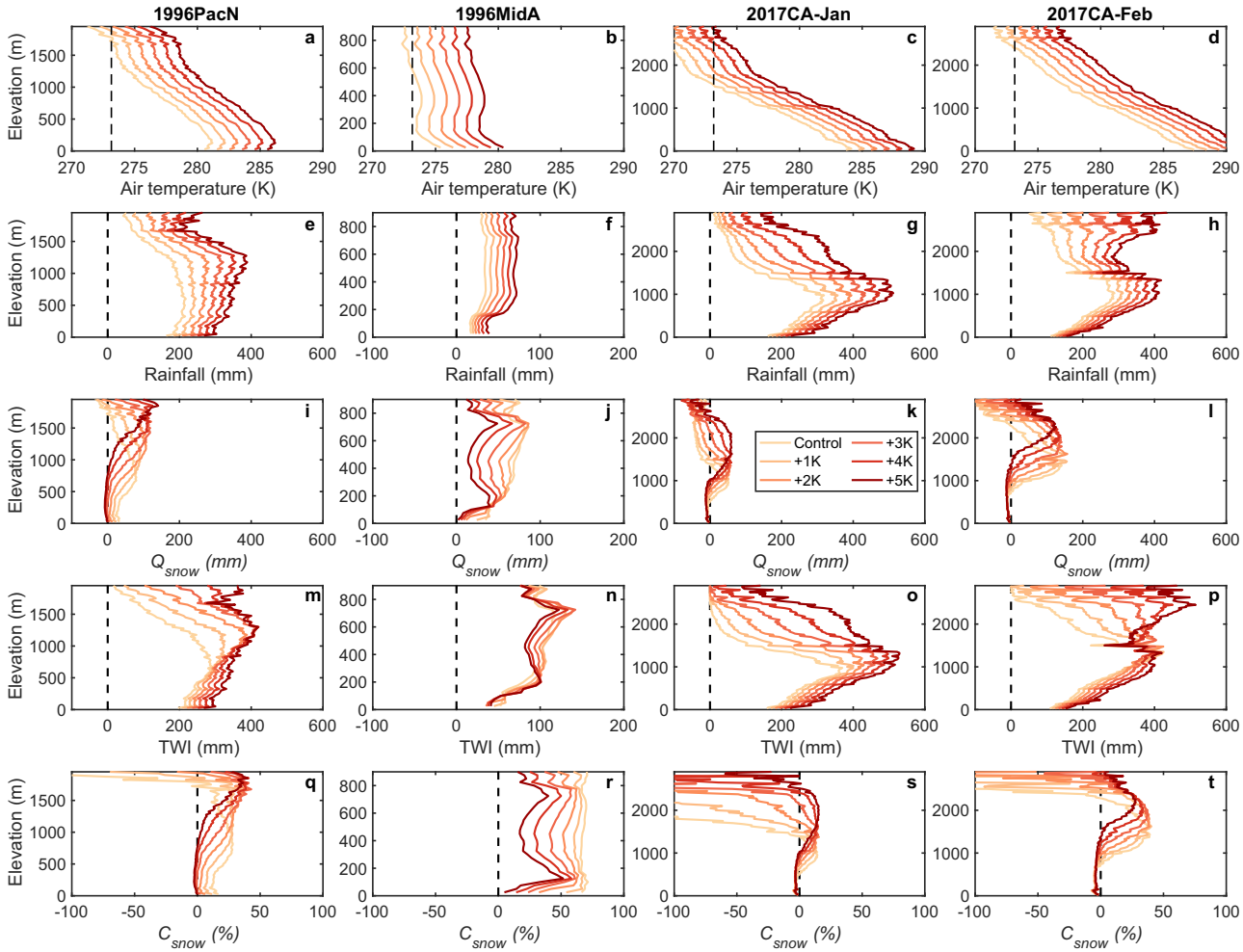

Fig. 3 | Elevation profiles of different variables for the four events: 1996PacN, 1996MidA, 2017CA-Jan, and 2017CA-Feb under the Control and warming scenarios. The first to fifth rows represent: **a-d**, air temperature; **e-h**, rainfall; **i-l**, sum of liquid water retention and snowmelt (Q_{snow}); **m-p**, terrestrial water input (TWI); and **q-t**, relative snow contribution to TWI (C_{snow}), respectively.

air temperature (Fig. 3q), mainly due to the increasing snowmelt in the high elevation regions with deep snowpack that survives despite warming. For 1996MidA, TWI shows a slight decrease with warming across all the elevation ranges (Fig. 3n), since the maximum elevation of the basin is relatively low (~ 800 m) (Figure S1), and warming has larger effects on antecedent snowpack (Figure S4). In this case, the increased rainfall offsets the reduced Q_{snow} (Fig. 3j, n, r). For 2017CA-Jan, TWI increases with warming across all the elevation ranges (Fig. 3o), mainly driven by the large increase of rainfall (Fig. 3g). C_{snow} increases notably with warming at high elevations and warming even changes the sign of C_{snow} from negative to positive at middle elevations (Fig. 3k), showing the increasing contribution of snowmelt with the increasing elevation. For 2017CA-Feb, TWI increases with warming especially at high elevations, due to the large increase of rainfall and snowmelt (Fig. 3h, l). Compared to 2017CA-Jan, 2017CA-Feb shows a large snowmelt contribution to runoff nearly across all the elevation ranges (Fig. 3k, l). Overall, TWI increases or shows a small change at low elevations due to increased rainfall but reduced Q_{snow}, while TWI increases notably due to the increase of both rainfall and Q_{snow} at high elevations. These indicate the shift of flood-generating regimes at both low and high elevations.

The responses of ROS flood drivers to warming are spatially heterogeneous for all four events (Figures S6 and S8). Overall, the regions with increasing TWI and C_{snow} have deep initial snowpack, while the snowpack in the regions with decreasing TWI is relatively shallow (Figure S4). Apart from 2017CA-Jan, the higher increase of air temperature leads to larger regions with decreasing TWI (Figure S8). If there is insufficient snowpack for melt, the regions with increasing TWI at a low warming level will show decreasing TWI at a high warming level, compared to the historical values (Figure S8). Specifically, 2017CA-Jan shows a considerable increase of TWI and C_{snow} with warming in the mountainous regions (Figures S6c and S8c), because warming increases the air temperature in these regions from below freezing during the historical events to above freezing in the warming scenarios (Figure S5c). These results show that how the regions respond to warming depends on the warming level, initial SWE, and local hydrometeorological conditions.

Divergent responses of runoff to warming

The basin-wide cumulative runoff shows distinct responses to warming (Fig. 4a). Both 1996PacN and 2017CA-Jan show a linear increasing trend with warming, and 2017CA-Jan has a higher increasing rate than 1996PacN. In contrast, under warming, runoff decreases for 1996MidA, while there is a non-monotonic trend for 2017CA-Feb. Specifically, for 2017CA-Feb, runoff first increases and then decreases with warming, with the maximum occurring in the +3 K scenario. For 1996PacN, runoff changes from 167.2 mm (Control) to 240.5 mm (+5 K), an increase of 44% as air temperature increases by 5 K, while 2017CA-Feb shows a similar increase of 40%. Runoff shows a large increase of more than 263% for 2017CA-Jan. In contrast, compared to the Control scenario, the +5 K scenario shows a large decrease in runoff for 1996MidA, reaching up to about 62%. This suggests that warmer climates may strengthen or reduce

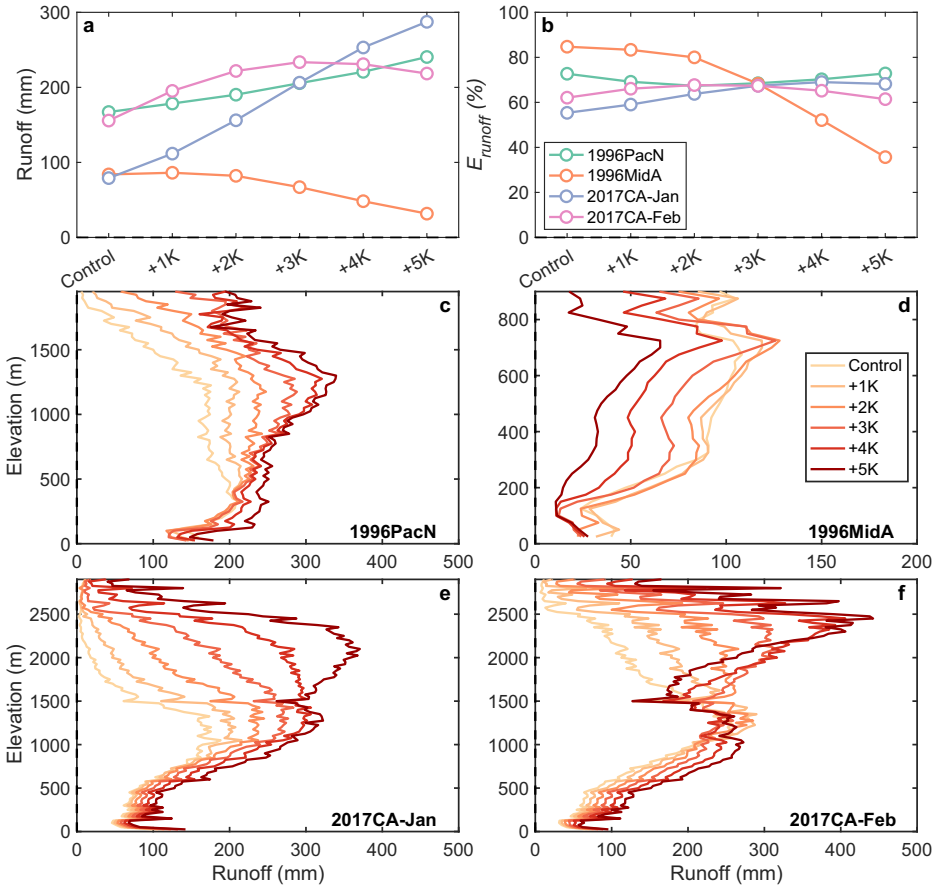

Fig. 4 | Responses of the basin average and elevation profiles of cumulative runoff and runoff efficiency for the four events in a warmer climate. **a** Basin average runoff under the control and warming scenarios. **b** Basin average runoff efficiency, defined as the ratio of runoff to terrestrial water input (TWI), under the Control and warming scenarios. **c-f** Elevation profiles of runoff for the four events: 1996PacN, 1996MidA, 2017CA-Jan, and 2017CA-Feb.

the ROS flooding intensity, depending on the warming level and specific event characteristics. Some historic extreme flood events may become more intense and destructive with warming, exacerbating flood control. Although the basin-wide runoff overall follows similar trends with TWI, 2017CA-Feb is the exception, where runoff first increases and then decreases with warming (Fig. 4a), while TWI monotonically increases with warming (Fig. 2c). This is because the runoff efficiency (defined as the ratio of total runoff to TWI) also changes with warming (Fig. 4b), due to soil thawing and change of antecedent soil moisture. Note that the definition of runoff efficiency in this study differs from the traditional one based on cumulative precipitation, considering that snowmelt is an important source of liquid water input during the ROS events. Apart from the cumulative runoff magnitude, warming also shifts the peak timing of runoff to earlier (Figure S9).

The runoff responses to warming are elevation-dependent (Fig. 4c-f) for all four events. Driven by the TWI change (Fig. 3m-p), runoff overall increases along the elevation profiles except for 1996MidA. This indicates that for 1996PacN, 2017CA-Jan, and 2017CA-Feb, the flood risks increase along the elevation profiles despite the elevation-dependent change in the flood-generating regimes. High elevations could experience unprecedented flood risks driven by both rainfall and snowmelt. For 1996PacN, compared to the Control scenario, the +5 K scenario shows a considerable runoff increase of over 100 mm at elevations above 850 m, with the largest increase of ~226 mm at 1850 m. For 2017CA-Jan, the runoff increases by more than 100 mm when the elevation is above 900 m, and the largest increase is 353 mm at around 2100 m. For 2017CA-Feb, the runoff increase is larger than 100 mm at elevations above 1900 m, with a maximum increase of 385 mm at around 2650 m. Over the regions above 1500 m, the runoff increase rates are 59%, 162%, and 13% per K for the three events. In contrast, the rates are 8%, 18%, and 4% per K over the regions below 1500 m. Due to relatively low elevations of <800 m, 1996MidA has a rate of −12% per K, showing a decreasing flood risk with warming.

The runoff responses to warming also show heterogeneous spatial patterns (Figure S11). Similar to TWI, high elevations with deep initial snowpack overall show a larger runoff increase under warming (Figure S12). The spatial patterns of runoff change are overall similar to those of TWI. However, the increasing TWI is not always associated with increasing runoff. For example, the south-central regions during 2017CA-Jan show an increasing TWI but decreasing runoff (Figure S12), due to increasing soil infiltration and percolation (Figure S10). This is because increased soil temperature thaws the soil ice (Figure S13), causing an increase in soil hydraulic conductivity[39]. Besides, the regions with decreasing TWI may exhibit increasing runoff (Figure S12). This can be explained by the increasing initial soil moisture before the events, making the soil wetter and saturated (Figure S14), thus driving the runoff increase. These showcase the importance of soil moisture in mediating the impactful flood responses to warming.

Altered water budget under warming

We further analyzed the basin-wide responses of different components in the water budget (see Methods) to decipher the underlying drivers of runoff change with warming. We define the sign of each component based on their contribution to runoff, with a positive value corresponding to an increase in runoff, while a negative value is related to a decrease in runoff. For example, a positive value of the change of snow water equivalent (ΔSnow) represents a loss of snowpack, which generates higher snowmelt and consequently more runoff. Overall, rainfall, snowfall, ΔSnow, and the change of water in the soil and unconfined aquifer (ΔSoil and ΔAquifer) determine the magnitude of runoff, while other components only account for relatively small proportions, for the four events (Fig. 5). The sum of rainfall, snowfall, and ΔSnow determines the TWI magnitude, while the sum of ΔSoil and ΔAquifer represents the infiltration and affects the runoff efficiency. For all four events, warming consistently increases rainfall and decreases snowfall. Compared to other events, snowfall during 2017CA-Jan accounts for a

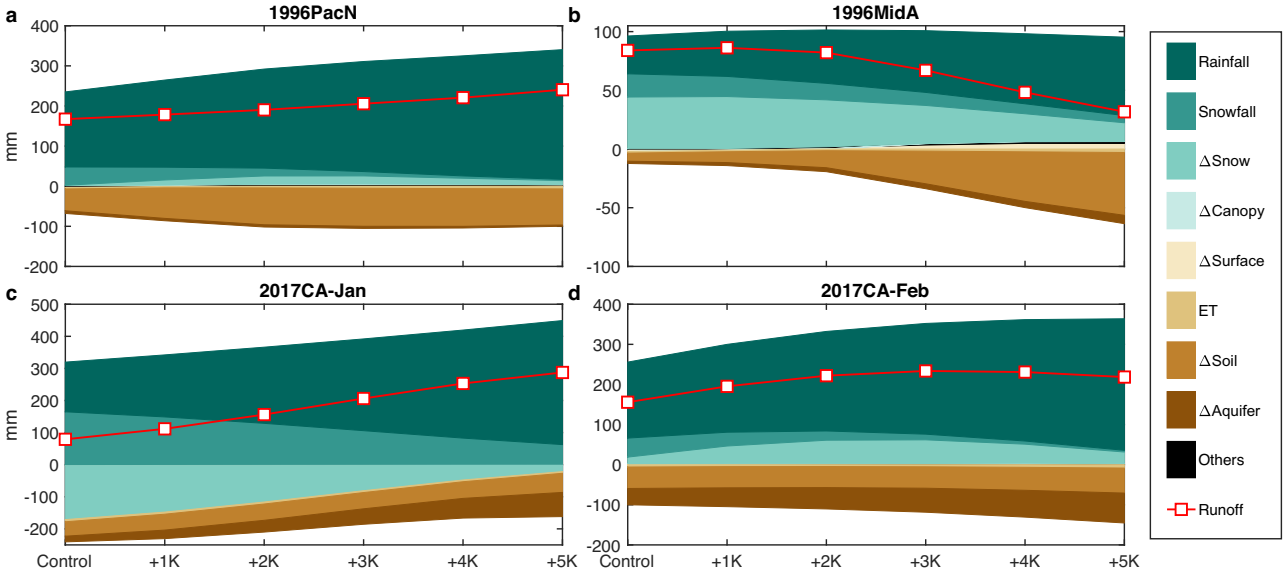

Fig. 5 | Changing water budget with warming during the ROS extreme flood events. a-d represent four different events: 1996PacN, 1996MidA, 2017CA-Jan, and 2017CA-Feb. In each panel, the height of color patch represents the cumulative magnitude for each component during the event, and the color patch above or below 0 represents that the associated component has positive or negative contribution to runoff, respectively. In the legend, ΔSnow, ΔCanopy, ΔSurface, ΔSoil, and ΔAquifer are the change of the water in snow, canopy (intercepted), surface, soil and unconfined aquifer; ET is the vegetation evapotranspiration and ground evaporation; and Others are the remaining runoff, e.g., from glaciers and lakes.

larger proportion (51%) of total precipitation in the Control scenario but it reduces to around 14% in the +5 K scenario (Fig. 5c), suggesting less snow accumulation during this event under warming. ΔSnow shows diverse changes with warming in the four events. Apart from 2017CA-Jan, ΔSnow increases runoff due to snowmelt in all the scenarios for all the other events. Notably, among them, 1996MidA shows a larger decrease of ΔSnow from 44 mm in the Control scenario to 16 mm in the +5 K scenario. The sum of ΔSoil and ΔAquifer overall increases with warming for all the events, reducing runoff intensity. Overall, different water budget components could show diverse changes with warming in terms of their sign, magnitude, and trend (Fig. 5).

The change in each component of the water budget explains the distinct responses of runoff for each event (Figs. 5 and 6). Overall, warming leads to increased rainfall, reduced snowfall, a diminished initial snowpack for snowmelt, and higher soil temperatures. If the change of initial soil moisture is small, as air temperatures transition from cooler to warmer, ROS-induced runoff could initially increase due to increasing rainfall and snowmelt, but subsequently decrease due to decreasing snowmelt caused by shallower initial snowpack and increasing soil infiltration caused by the thawing soil (Fig. 6). However, the specific responses of runoff for each event to warming depend on its unique hydrometeorological conditions and the relative change of different water components under warming. For 1996PacN, the increase of runoff with warming is mainly by the increases of ΔRain (Fig. 5a). For 1996MidA, despite the increasing rainfall, the decrease of ΔSnow and increase of ΔSoil jointly determine the larger decrease of runoff under warming (Fig. 5b). For 2017CA-Jan, the runoff increase is mainly determined by the increase of rainfall and the decrease of ΔSnow, related to reduced snow accumulation and increasing snowmelt during the event (Fig. 5c). For 2017CA-Feb, the non-linear responses of ΔSnow and change of rainfall, ΔSoil and ΔAquifer affect the runoff trend under warming (Fig. 5d). These underscore the importance of scrutinizing the change of each component in the water budget when forecasting and managing ROS-induced extreme flood risks.

Discussion

We reproduced four past ROS extreme flood events with a kilometer-scale land surface model. Compared to the coarse-scale simulations, the kilometer-scale ELM simulations enable us to better capture the fine-scale spatial details and elevation dependence of ROS events. The uncertainty of atmospheric forcing has considerable impacts on the snowpack[40,41] and runoff simulations (Table S5). The temporal downscaling (see Methods) of daily atmospheric forcings can potentially affect simulated runoff responses during ROS events, particularly the timing and magnitude of peak runoff [42]. However, our simulations show good agreement with field measurements (Figure S3). Moreover, since our study primarily focuses on event-scale responses of cumulative TWI and runoff, we expect temporal downscaling to have a limited impact on our results, as demonstrated by ref. 42. Our model calibration and evaluation also suggest that the global parameter settings in land surface models can bias regional and event-scale study. Regionalizing the parameters in the runoff and snowpack simulations is essential, as demonstrated by ref. 43,44. The hindcast simulations show that the contribution of snow (i.e., liquid water retention and snowmelt) to flooding varies with the events. Differences in the estimated C_{snow} among studies may be caused by differences in the model structure, and the vertical flow assumptions between preferential flow and matrix flow (assumed in ELM)[45,46] as well as the inconsistencies in the coverage of the study basins and specific date range. Although assuming the matrix flow rather than preferential flow may overestimate the snowmelt contribution[29], the measurements in ref. 47. showed that the preferential flow only accounts for a small volume (about 3-8%) of the overall snowpack, and there is still limited knowledge of how, when, and where preferential flow forms and distributes[2]. Although ELM neglects the advected heat from rain into snow, the impacts are expected to be limited[48], considering that the advected heat transfer only shows a small contribution of <5% to snowmelt in the ROS events over CONUS[5]. Our analyses primarily focus on the relative differences between storylines, mitigating the impact of model uncertainties.

Using a storyline approach, we examined how four selected extreme flood events caused by ROS would unfold and how major flood drivers would change in a warmer climate. Our results suggest the diverse responses of different ROS-induced extreme flood events to a warmer climate. The trend of runoff in response to warming can be nonlinear and non-monotonic (Fig. 4a), corroborating previous findings[25]. A similar non-monotonic response to warming temperatures has also been reported for peak seasonal streamflows in snow regions[49,50]. The runoff response is jointly

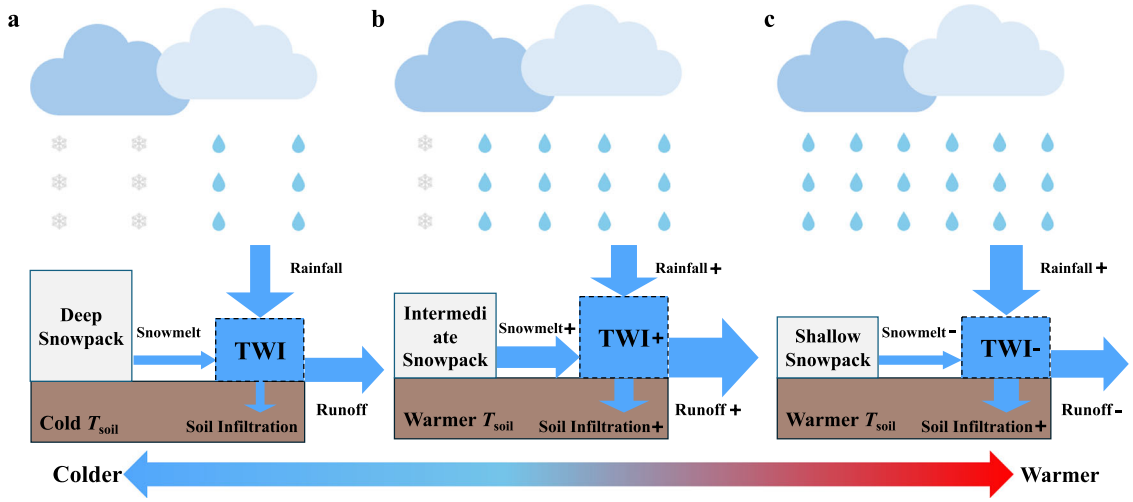

Fig. 6 | Conceptual schematic illustrating the changes in water budget during rain-on-snow events under varying air temperatures. Panels **a-c** represent increasing air temperatures. Warmer air temperatures drive runoff change by increasing rainfall, decreasing snowfall, decreasing initial snowpack for snowmelt, changing snowmelt, and increasing soil temperature (T_{soil}) and thus soil infiltration. Note that with larger warming from panel **b** to panel **c**, runoff may increase if increasing rainfall shows a dominant role, e.g., in 1996PacN, and snowmelt contributions may still increase due to the cold air temperature during the historical events, e.g., in 2017CA-Jan. Here we assume that the potential changes of initial soil moisture before the events is small and the precipitation scaling of +7% per K is uniform across space and time, but the potential spatial and temporal changes of initial soil moisture and precipitation scaling can complicate the responses of soil infiltration and runoff to warming.

driven by the change of TWI and altered soil infiltration. The TWI responses are affected by the complicated snowpack-rainfall interaction[37,51]. The soil infiltration is affected by initial soil moisture and soil freezing-thawing process. The soil moisture memory effects can potentially increase runoff[29], while less frozen soil under warming will reduce runoff due to increased soil permeability[23]. All the water budget components change with warming in different ways[23] and contribute to the distinct runoff responses (Fig. 6), posing challenges for accurate flood forecasting. Notably, some historic extreme events could become more severe with warming. For example, 2017CA-Feb will have a larger runoff under all the warming scenarios than the Control scenarios (Fig. 4a), with a rate of 8% per K. Considering that the Oroville Dam was already threatened by 2017CA-Feb[9], it will face higher risks under warming with potential societal and economic impacts on the surrounding largest metropolitan regions. Notably, the runoff increase rate is around 53% per K for 2017CA-Jan, representing a notably increasing flood potential with warming. Besides, warmer temperatures will shift peak timing to earlier for all the events, in line with ref. 25. These understandings and the storyline-based framework will be helpful for decision-makers to better project and manage extreme floods from ROS under global warming.

Warming alters the flood-generating regimes along the elevation profiles. The joint increase of rainfall and snowmelt with warming considerably increases TWI and runoff at high elevations during extreme events (Figs. 3 and 4). Consequently, high elevations may experience unprecedented floods in a warmer climate, although they have experienced a relatively small flood risk from historical events. In the control scenario, the deep, cold snowpack at high elevations buffers the rainfall and reduces runoff, as the unsaturated snowpack can retain more liquid water, and the large cold snowpack may refreeze the liquid rain[37]. However, the decrease in SWE with warming reduces the effects of snow buffering. Besides, increasing air temperature also increases the rainfall probability and provides more longwave radiation for snowmelt. The regions above 1500 m show a considerable increase of runoff with a rate of 59%, 162%, and 13% per K, respectively, for 1996PacN, 2017CA-Jan, and 2017CA-Feb, demonstrating a considerable increasing flood risk with warming. In contrast, low elevations could experience a shift in the flood regime from ROS-driven to rainfall-dominated due to the increasing rainfall and diminished snowmelt caused by the decrease of the total available snowpack for melting. It should be noted that TWI and runoff at low elevations do not necessarily decrease under a warmer climate due to the increasing extreme precipitation and higher rain probability. The elevation-dependent patterns are also found in the large-scale climate simulations, which projected an increase in ROS risks at high elevations under the scenario of Representative Concentration Pathway 8.5[20]. Therefore, warming could considerably increase the flood risks of ROS-induced extreme flood events at high elevations in terms of runoff. The elevation-dependent shift can potentially cause impacts to the infrastructure and people in regions that are not typically flood-prone historically, challenging the current flood control and reservoir management systems. Note that since runoff from high elevations affects streamflow at low elevations, the flood risk at low elevations is not necessarily lowered, even if they may experience reduced runoff under warming.

The extreme precipitation change has straightforward impacts on TWI and thus runoff. The extreme precipitation increase aggravates the flood risks along the elevation profiles for all the events (Figs. 3 and 4). Although there are large differences in the projected mean precipitation among Earth system models (ESMs)[52,53], the extreme precipitation projection at short durations is generally expected to increase with warming by about +7% per K[54–56], motivating the construction of the scenarios used in the study (see Methods). However, the precipitation increase rate can be faster than +7% per K due to the positive feedback between precipitation and updraft[57]. In this case, our scenarios will underestimate the future flood risks along the elevation profiles because our simulations did not include an active atmosphere model. The uniform precipitation scaling of +7% per K across space and time in our simulations is another source of uncertainty. The precipitation scaling rate has been demonstrated to exhibit spatial[58,59] and temporal[60,61] heterogeneity, which could impact the spatio-temporal distribution of precipitation intensity and further complicate the runoff responses during ROS events. Despite the aforementioned potential uncertainty sources, further exploration of the storyline simulations without precipitation change shows that although assuming the precipitation change or not can impact simulated initial soil moisture (Figure S15) and soil infiltration (Figure S16), the runoff responses to warming and the associated elevation profiles overall remain unchanged (Figures S17-S18). These additional analyses provide a consistent conclusion (Figures S15-S18), which suggests the generalizability of our results.

We focus on understanding the well-known ROS-induced extreme flood events and their plausible analogs in a warmer climate, rather than

estimating the occurrence and frequency of the extreme events. The storyline realizations are dynamically consistent with the meteorological conditions during the observed historical extreme events, thus avoiding the uncertainties in the climate change projections. Although Earth system models (ESMs) (e.g., those involved in the Coupled Model Intercomparison Project Phase 6[62]) can provide spatially- and temporally-varying future climate information, their spatial resolution (≥1°) is too coarse to capture the spatial details of the extreme events especially over mountains[63]. The spatial downscaling techniques can be used to improve the spatial resolution of ESM outputs, however, the accuracy of the downscaled data is affected jointly by the biases of ESM outputs and uncertainties from the downscaling techniques[64]. Besides, ESMs also show poor performance and large variabilities in capturing extreme precipitation[65] and snowpack evolution[66]. How to weigh or subset the multi-model ensembles to get reliable projections of ROS is still an unresolved issue[67], which is beyond the objective of this study. Therefore, the study used the alternative storyline approach[5] to construct the warming scenarios with a uniform increase of air temperature and the associated precipitation change, which preserved the observed hydrometeorological characteristics of the historic events. We acknowledge that continued advancements in Earth system modeling will progressively enhance our capacity to project the occurrence, frequency, and severity of ROS extreme flood events in a warmer climate.

We quantified the sensitivity of selected ROS extreme flood events to warming and examined the physical processes and drivers responsible for the plausible change under a warmer climate (Fig. 6). These event-based kilometer-scale sensitivity tests and process-based understandings will be promising to support the evaluation of potential damages and losses due to similar impactful ROS flood events. Given that global warming is altering the ROS characteristics, shifting the elevation-dependent flood regimes and the associated flood risks over different parts of the globe including High Mountain Asia[68], China[69], Europe[70,71], and global mountains[72], follow-up work may explore storyline-based scenarios for other high-risk ROS events in global snow regions, e.g., the California New Year's flood event of 1997[26,27], Yellowstone flood event of 2022[73]. Beyond the short-term flooding impacts, these ROS extreme flood events can further lead to snow droughts and increase nutrient loading in coastal and estuarine zones, deserving future investigation.

Methods

Drivers of four historic ROS extreme flood events

1996PacN was driven by the concurrence of an antecedent deep snowpack and a strong, warm atmospheric river with record-breaking rain. Specifically, before the 1996PacN event, below-freezing air temperature and heavy snowfall resulted in a considerable snowpack accumulation in the lower-elevation areas over the Willamette basin of the Pacific Northwest region (Figure S2a). Then, a series of landfalling Pacific atmospheric rivers during Feb 5-9, 1996 caused intense rainfall, and the accompanying warm air temperature further augmented the flooding by accelerating snow ablation[6].

1996MidA was caused by a deep snowpack that formed due to a cold start to the winter and several snowstorms, followed by a rapid rise in temperature and heavy rainfall from a synoptic-scale storm system. Specifically, combined with continuous low air temperature prior to the event, a succession of winter snowstorms created an unusually deep snowpack over the Susquehanna River Basin of the mid-Atlantic region (Figure S2b). Moving through the eastern US from Jan 17 to 20, 1996, a strong synoptic-scale storm system brought heavy rainfall and also initiated the warm conditions for rapid snowmelt[7], which produced the record-setting flash flooding.

Both 2017CA-Jan and 2017CA-Feb were driven by atmospheric rivers with prolonged, intense rainfall, but the second event was warmer. Specifically, two storm sequences associated with the atmospheric rivers triggered persistent extreme precipitation and brought warm conditions for snowmelt over the Feather, Yuba, and American River basins of Sierra Nevada (Figure S2c), including an earlier one during Jan 7-12, 2017 (hereafter 2017CA-Jan) and a later one from Feb 6 to 12 (2017CA-Feb)[29]. This extreme event generated excessive and rapid runoff into Lake Oroville and caused the 2017 Oroville Dam spillways incident[74].

Kilometer-scale ELM simulations

E3SM, supported by the US Department of Energy, targets to improve actionable predictions of variability and change of the Earth system by optimizing the use of the leading-edge computational resources for ultra high-resolution modeling[75]. As the land component of E3SM, ELM is sourced from the Community Land Model version 4.5 (CLM4.5)[32,76]. We used the latest released version 3 of ELM (ELM3) in the study. Compared to its predecessor, ELM3 adds some new features or options, e.g., a new parameterization for the sub-grid topographic effects on solar radiation[77], improved snow radiative transfer schemes[78]. Recently, we also developed a suite of 1 km land surface parameters for supporting ultra-high-resolution (e.g., 1 km) land surface and Earth system modeling[79]. These advancements allow us to use ELM to perform 1 km ROS simulations.

ELM has been widely used in snowpack simulations and projections[15,80] and runoff generation[43]. ELM uses a mechanistically-based multi-layer snow scheme to simulate various snow processes (e.g., snow accumulation, snow aging, snowmelt). Although ELM can overall capture the spatio-temporal patterns, interannual variability and elevation profiles of SWE, optimizing the ELM parameters is vital for accurately simulating SWE[80]. By default, ELM uses a simple TOPMODEL-based scheme with global constant parameters for producing surface and subsurface runoff[18]. However, model calibration is essential to reduce the parametric uncertainty and improve the performance for runoff simulations when applying to a specific basin/region[43]. Therefore, recalibrating ELM runoff- and snowpack-related parameters is necessary for better reproducing ROS flood events.

Benchmark datasets

We collected daily field measurements and reanalysis datasets (Table S1) for model calibration, evaluation and intercomparison covering the three basins (Fig. 1).

For snowpack, we used the daily SWE observations from the Bias Correction and Quality Control SNOTEL data[81] for the model calibration of 1996PacN and 2017CA. Considering that SNOTEL sites are only distributed in the western US, we used the Northern Hemisphere Snow Water Equivalent (NH-SWE) dataset for 1996MidA. NH-SWE provides the daily SWE time series converted from the in-situ snow depth data[82]. We also collected the daily 4 km gridded SWE data over CONUS developed by the University of Arizona (UA)[83] for the intercomparison.

For runoff, we used the daily 5 km GRFR runoff dataset as a benchmark. GRFR is generated using the Variable Infiltration Capacity model with grid-scale parameter calibration and bias correction and shows good capabilities of capturing extreme flood events[36]. Besides, we also collected the daily USGS streamflow observations for an independent evaluation across the "reference" gauges from the Geospatial Attributes for Gauges for Evaluating Streamflow (GAGES-II) data set[84].

Model calibration, evaluation, and hindcast ROS simulations

Atmospheric forcings play a big role in the snowpack and runoff simulations of land surface models[40]. We first collected four high-spatial-resolution atmospheric forcing data including: the hourly 0.125° North American Land Data Assimilation System phase 2 (NLDAS-2)[85], daily 1/16° spatially comprehensive, hydrometeorological data set for Mexico, the U.S., and Southern Canada (L15)[86], daily 1 km Daymet[87], and daily 4 km Parameter-elevation Regressions on Independent Slopes Model (PRISM)[88]. We temporally downscaled the daily data from L15, PRISM and Daymet data into hourly data using the Mountain Microclimate Simulation Model[89]. Specifically, we first determined the timing of daily maximum and minimum air temperatures, and then interpolated the hourly time series using a spline function. We also distributed daily total precipitation into equal hourly values. We further spatially downscaled the NLDAS-2, L15 and PRISM data to 1 km using the bilinear interpolation methods. Note that L15 only provides precipitation,

air temperature and wind data, while Daymet and PRISM only contain precipitation and air temperature data. We incorporated other variables from NLDAS-2 into these three forcing data.

We performed the simulations of the ROS extreme flood events, driven by the four different atmospheric forcings, using ELM with 1 km land surface parameters from ref. 79. and default model configurations. Then focusing on the two months encompassing the events, we evaluated the ELM performance on simulating snowpack and runoff against field measurements in terms of the correlation coefficient (R), root mean square error (RMSE) and mean bias on a daily scale. Specifically, we compared simulated daily SWE with SNOTEL observations and NH-SWE data at the available sites, and compared simulated basin-averaged runoff with that from GRFR data. Finally, we determined the optimal atmospheric forcing with the best performance separately for each region. Note that the same forcings were used for two 2017CA events.

We identified and calibrated the sensitive ELM parameters for snowpack and runoff simulations for each individual region (Tables S3, S4). For snowpack, the local sensitivity analysis showed that snowfall temperature (T_{fall}) and snow freezing temperature (T_{freeze}) have large impacts on SWE simulations, while other parameters, including the tuning parameter for top snow/soil layer thickness, and snow cover accumulation and depletion curve shape parameters, have negligible impacts. Note that ELM uses an air temperature-based linear scheme to separate total precipitation into rainfall and snowfall. It is to be noted that while varied methods for determination of precipitation as snow or rain has been proposed[90], temperature-based methods have shown widespread success[91]. We defined the threshold air temperature at which the snow vs. rain probability is 50% as T_{fall}. The precipitation falls either as rain or snow when air temperature is above T_{fall} + 1 K or below T_{fall}-1 K, and there is a mix of rain and snow for intermediate air temperature. The default value of T_{fall} is 274.15 K (1 °C) in ELM, and as T_{all} has been found to vary spatially[92], we selected it as one of the sensitive parameters. For runoff, we selected the decay factor for surface runoff (f_{over}) and decay factor for subsurface runoff (f_{drai}) as the two most sensitive parameters according to ref. 43. We first performed the ELM simulations with all the combinations of T_{fall} and T_{freeze}, and then determined the optimal parameters based on the minimum RMSE between simulated and measured SWE for each region. We then ran ELM with the optimal snowpack parameters and all the combinations of f_{over} and f_{drai}. The runoff evaluation based on the minimum RMSE was used to determine the optimal runoff parameters for each region.

Finally, we performed the ELM hindcast (Control) simulations with the region-specific optimal atmospheric forcings and calibrated snowpack- and runoff-related parameter settings (Table S4). Note that for model initialization, we ran ELM starting 30 years before the events. Then we evaluated the ELM simulations using the SNOTEL measurements, NH-SWE data and USGS streamflow observations at a daily scale. Note that we did not perform the river routing and used the aggregated daily runoff over the drainage area for each gauge to approximate the streamflow. Although there is a possible timing shift between the routed streamflow and aggregated runoff, but ref. 5. demonstrated that these two at the daily scale showed the modest difference over CONUS.

ROS storyline simulations under warmer scenarios

We constructed the future storylines using the delta warming approach, which has been widely used to analyze the sensitivity of snowmelt[49,93,94] and ROS[5,95] to increasing air temperature. Specifically, the five warming storylines assume the increase of air temperature from +1 K to +5 K at a 1 K interval, considering that the air temperature is projected to increase by +1 K and +5 K approximately at the end of the 21st century under the optimistic low-emission and the "business as usual" scenarios over CONUS[34], respectively.

For each storyline, we perturbed the hourly air temperature (T_{air}; unit: K) with the ΔT_{air} K in the historical atmospheric forcing data. We updated the hourly downward longwave radiation (R^{Δ}_{Long}) with the assumption of unchanged atmospheric emissivity (e_{air}) as:

$$R^{\Delta}_{Long} = e_{air} \cdot \sigma \cdot (T_{air} + \Delta T_{air})^4 \tag{1}$$

where s is the Stefan–Boltzmann constant. e_{air} can be derived by:

$$e_{air} = \frac{R^{0}_{Long}}{\sigma \cdot (T_{air})^4} \tag{2}$$

where R^{0}_{Long} is the downward longwave radiation in the historical data.

Following ref. 93, we kept hourly relative humidity in the warming storylines the same as that in the historical atmospheric forcing data, to permit the variability of water vapor pressure in a way in line with the ideal gas. Thus, the water vapor pressure (e_{Δ}) under the warmer storylines was derived based on the August–Roche–Magnus formula[96]:

$$\begin{aligned} e_{\Delta} &= RH \cdot e^{s}_{\Delta} = e_0 \frac{e^{s}_{\Delta}}{e^{s}_{0}} \\ &= e_0 \frac{\exp(17.641 \cdot (T_{air} + \Delta T_{air} - 273.15)/(243.27 + T_{air} + \Delta T_{air} - 273.15))}{\exp(17.641 \cdot (T_{air} - 273.15)/(243.27 + T_{air} - 273.15))} \end{aligned} \tag{3}$$

where RH is the relativity humidity, e^{s}_{0} and e^{s}_{Δ} are the saturation water vapor pressure at the historical data and warmer storylines, respectively, and e_0 is the water vapor pressure in the historical data. Then, the specific humidity (q_{Δ}) was calculated via

$$q_{\Delta} = \frac{d \cdot e_{\Delta}}{p - (1 - d) \cdot e_{\Delta}} \tag{4}$$

where d is the molar mass ratio of water vapor to dry air, which is a constant of 0.622, and p is the total atmospheric pressure.

As air temperature increases, the water holding capacity of air increases at a rate of about +7% per K according to the Clausius–Clapeyron relationship[35]. Both the observations[61] and ESM simulations[54] support that extreme precipitation at short durations approximately follows this rate. Therefore, we adjusted the extreme precipitation (P_{Δ}) as

$$P_{\Delta} = P_0 \cdot (1 + \alpha)^{\Delta T_{air}} \tag{5}$$

where P_0 is the precipitation in the historical data, and the scaling rate α is set as +7% per K uniformly across space and time in the study.

We ran plausible future simulations using ELM driven by the updated atmospheric forcings under different warmer storylines. Besides, we also ran another set of future ELM simulations without precipitation change, to separate the impacts of warming-induced precipitation change from increasing air temperature. Note that we ran ELM starting from the beginning of the previous year of the events (one year earlier). This way, we generated the initial conditions before the events with respect to the warmer climate.

Analyzing sensitivity of ROS floods to warming

Using both the hindcast and plausible future simulations, we analyzed the basin-wide and grid-scale sensitivity of the four ROS flood events to a warmer climate in terms of magnitude, peak timing, spatial variations, and elevation profiles. We used runoff to quantify and evaluate future flood risks of ROS, following ref. 5. We also quantified the change of rainfall and snow contribution. We defined TWI as the total liquid water input into soil during the event, primarily contributed by rainfall and snowmelt. TWI could be smaller than rainfall, due to the complicated interaction between rainfall and snowpack especially for regions with deep snowpack[37]. Therefore,

we calculated the relative contribution of snow by

$$C_{snow} = \frac{Q_{snow}}{TWI} = 1 - \frac{Q_{rainfall}}{TWI} \quad (6)$$

where Q_{snow} represents the sum of liquid water retention and snowmelt, and $Q_{rainfall}$ is the rainfall. Note that C_{snow} can be smaller than 0, showing that snowpack reduces rainfall and thus TWI, while $C_{snow} > 0$ indicates a positive snow contribution to TWI. We further analyzed the response of runoff to warming. To unravel the underlying mechanisms, we quantified the contributions of the change of each component in the water budget to the change of runoff:

$$\Delta W_{canopy} + \Delta W_{surface} + \Delta W_{snow} + \Delta W_{soil} + \Delta W_a = \left(\frac{Q_{rainfall} + Q_{snowfall} - ET}{-Q_{runoff} - Q_{others}} \right) \cdot \Delta t \quad (7)$$

where the left five terms represent the changes in canopy water (liquid +solid), surface water, snow water, soil water, and unconfined aquifer water. In the right part of the equation, and $Q_{snowfall}$ is the snowfall, ET is the sum of vegetation evapotranspiration and ground evaporation, Q_{runoff} is the total runoff from surface and subsurface, Q_{others} represents other runoff from glaciers, lakes and others, and Δt is the time step.

Besides, we also compared the storyline simulations with and without precipitation change to quantify the impacts of precipitation change.

Data availability

All the benchmark datasets used in the study are openly accessible via the links listed in Table S1. The model outputs from the ELM simulations used in the study are available at https://doi.org/10.5281/zenodo.14545539.

Code availability

The ELM code can be freely downloaded at https://github.com/E3SM-Project/E3SM. Scripts to reproduce all results and plot all figures are publicly accessible at https://github.com/daleihao/ROS_Flood_Extremes.

Received: 3 January 2025; Accepted: 1 May 2025;
Published online: 24 May 2025

References

1. Zhou, Y. et al. Atmospheric river frequency-category characteristics shape U.S. West Coast Runoff. *J. Geophys. Res. Atmos.* **130**, e2024JD041805 (2025).
2. Brandt, W. T., Haleakala, K., Hatchett, B. J. & Pan, M. A review of the hydrologic response mechanisms during mountain rain-on-snow. *Front. Earth Sci.* **10**, 791760 (2022).
3. Wayand, N. E., Lundquist, J. D. & Clark, M. P. Modeling the influence of hypsometry, vegetation, and storm energy on snowmelt contributions to basins during rain-on-snow floods. *Water Resour. Res.* **51**, 8551–8569 (2015).
4. McCabe, G. J., Clark, M. P. & Hay, L. E. Rain-on-snow events in the Western United States. *Bull. Am. Meteorol. Soc.* **88**, 319–328 (2007).
5. Li, D., Lettenmaier, D. P., Margulis, S. A. & Andreadis, K. The role of rain-on-snow in flooding over the Conterminous United States. *Water Resour. Res.* **55**, 8492–8513 (2019).
6. Colle, B. A. & Mass, C. F. The 5–9 February 1996 flooding event over the Pacific Northwest: sensitivity studies and evaluation of the MM5 precipitation forecasts. *Mon. Weather Rev.* **128**, 593–617 (2000).
7. Leathers, D. J., Kluck, D. R. & Kroczynski, S. The severe flooding event of January 1996 across North-Central Pennsylvania. *Bull. Am. Meteorol. Soc.* **79**, 785–798 (1998).
8. Zarzycki, C. M., Ascher, B. D., Rhoades, A. M. & McCrary, R. R. Algorithmically detected rain-on-snow flood events in different climate datasets: a case study of the Susquehanna River basin. *Nat. Hazards Earth Syst. Sci.* **24**, 3315–3335 (2024).
9. Vahedifard, F., AghaKouchak, A., Ragno, E., Shahrokhabadi, S. & Mallakpour, I. Lessons from the Oroville dam. *Science* **355**, 1139–1140 (2017).
10. Tarouilly, E., Li, D. & Lettenmaier, D. P. Western U.S. superfloods in the recent instrumental record. *Water Resour. Res.* **57**, e2020WR029287 (2021).
11. Räisänen, J. Warmer climate: less or more snow?. *Clim. Dyn.* **30**, 307–319 (2008).
12. Lettenmaier, D. P. & Gan, T. Y. Hydrologic sensitivities of the Sacramento-San Joaquin River Basin, California, to global warming. *Water Resour. Res.* **26**, 69–86 (1990).
13. Pendergrass, A. G. What precipitation is extreme?. *Science* **360**, 1072–1073 (2018).
14. Trenberth, K. E., Dai, A., Rasmussen, R. M. & Parsons, D. B. The changing character of precipitation. *Bull. Am. Meteorol. Soc.* **84**, 1205–1218 (2003).
15. Hao, D. et al. A cleaner snow future mitigates Northern Hemisphere snowpack loss from warming. *Nat. Commun.* **14**, 6074 (2023).
16. Rhoades, A. M. et al. Asymmetric emergence of low-to-no snow in the midlatitudes of the American Cordillera. *Nat. Clim. Change* **12**, 1151–1159 (2022).
17. Huang, H. et al. Changes in mechanisms and characteristics of western U.S. floods over the last sixty years. *Geophys. Res. Lett.* **49**, e2021GL097022 (2022).
18. Wachowicz, L. J., Mote, T. L. & Henderson, G. R. A rain on snow climatology and temporal analysis for the eastern United States. *Phys. Geogr.* **41**, 54–69 (2020).
19. Cohen, J., Ye, H. & Jones, J. Trends and variability in rain-on-snow events. *Geophys. Res. Lett.* **42**, 7115–7122 (2015).
20. Musselman, K. N. et al. Projected increases and shifts in rain-on-snow flood risk over western North America. *Nat. Clim. Change* **8**, 808–812 (2018).
21. Shepherd, T. G. et al. Storylines: an alternative approach to representing uncertainty in physical aspects of climate change. *Clim. Change* **151**, 555–571 (2018).
22. Trok, J. T., Barnes, E. A., Davenport, F. V. & Diffenbaugh, N. S. Machine learning–based extreme event attribution. *Sci. Adv.* **10**, eadl3242 (2024).
23. Baulenas, E., Versteeg, G., Terrado, M., Mindlin, J. & Bojovic, D. Assembling the climate story: use of storyline approaches in climate-related science. *Glob. Chall.* **7**, 2200183 (2023).
24. Sillmann, J. et al. Event-based storylines to address climate risk. *Earth's. Future* **9**, e2020EF001783 (2021).
25. Pettett, A. & Zarzycki, C. M. The 1996 Mid-Atlantic winter flood: exploring climate risk through a storyline approach. *J. Hydrometeorol.* **24**, 2259–2280 (2023).
26. Rhoades, A. M. et al. Recreating the California New Year's Flood Event of 1997 in a regionally refined earth system model. *J. Adv. Model. Earth Syst.* **15**, e2023MS003793 (2023).
27. Rhoades, A. M. et al. Anticipating how rain-on-snow events will change through the 21st century: lessons from the 1997 new year's flood event (2024).
28. Marks, D., Kimball, J., Tingey, D. & Link, T. The sensitivity of snowmelt processes to climate conditions and forest cover during rain-on-snow: a case study of the 1996 Pacific Northwest flood. *Hydrol. Process.* **12**, 1569–1587 (1998).
29. Haleakala, K. et al. Watershed memory amplified the Oroville rain-on-snow flood of February 2017. *PNAS Nexus* **2**, https://doi.org/10.1093/pnasnexus/pgac295 (2022).
30. Henn, B., Musselman, K. N., Lestak, L., Ralph, F. M. & Molotch, N. P. Extreme Runoff Generation From Atmospheric River Driven Snowmelt During the 2017 Oroville Dam Spillways Incident. *Geophys. Res. Lett.* **47**, e2020GL088189 (2020).

31. Haeffner, M. & Hellman, D. The social geometry of collaborative flood risk management: a hydrosocial case study of Tillamook County, Oregon. *Nat. Hazards* **103**, 3303–3325 (2020).
32. Golaz, J. C. et al. The DOE E3SM Model Version 2: overview of the physical model and initial model evaluation. *J. Adv. Model. Earth Syst.* **14**, e2022MS003156 (2022).
33. Hyman-Rabeler, K. A. & Loheide, I. I. S. P. Drivers of Variation in Winter and Spring Groundwater Recharge: Impacts of Midwinter Melt Events and Subsequent Freezeback. *Water Resour. Res.* **59**, e2022WR032733 (2023).
34. Crimmins, A. R. et al. *USGCRP, 2023: Fifth National Climate Assessment*. edn, (U.S. Global Change Research Program, 2023).
35. Boer, G. Climate change and the regulation of the surface moisture and energy budgets. *Clim. Dyn.* **8**, 225–239 (1993).
36. Yang, Y. et al. Global reach-level 3-hourly river flood reanalysis (1980–2019). *Bull. Am. Meteorol. Soc.* **102**, E2086–E2105 (2021).
37. Katz, L. et al. Antecedent snowpack cold content alters the hydrologic response to extreme rain-on-snow events. *J. Hydrometeorol.* **24**, 1825–1846 (2023).
38. O'Gorman, P. A. Contrasting responses of mean and extreme snowfall to climate change. *Nature* **512**, 416–418 (2014).
39. Xu, D. et al. Climate change will reduce North American inland wetland areas and disrupt their seasonal regimes. *Nat. Commun.* **15**, 2438 (2024).
40. He, C. et al. Can Convection-permitting modeling provide decent precipitation for offline high-resolution snowpack simulations over mountains?. *J. Geophys. Res.: Atmos.* **124**, 12631–12654 (2019).
41. te Linde, A. H., Aerts, J. C. J. H., Hurkmans, R. T. W. L. & Eberle, M. Comparing model performance of two rainfall-runoff models in the Rhine basin using different atmospheric forcing data sets. *Hydrol. Earth Syst. Sci.* **12**, 943–957 (2008).
42. Acharya, S. C., Nathan, R., Wang, Q. J. & Su, C.-H. Temporal disaggregation of daily rainfall measurements using regional reanalysis for hydrological applications. *J. Hydrol.* **610**, 127867 (2022).
43. Xu, D., Bisht, G., Sargsyan, K., Liao, C. & Leung, L. R. Using a surrogate-assisted Bayesian framework to calibrate the runoff-generation scheme in the Energy Exascale Earth System Model (E3SM) v1. *Geosci. Model Dev.* **15**, 5021–5043 (2022).
44. Tuo, Y., Marcolini, G., Disse, M. & Chiogna, G. Calibration of snow parameters in SWAT: comparison of three approaches in the Upper Adige River basin (Italy). *Hydrol. Sci. J.* **63**, 657–678 (2018).
45. Würzer, S., Wever, N., Juras, R., Lehning, M. & Jonas, T. Modelling liquid water transport in snow under rain-on-snow conditions—considering preferential flow. *Hydrol. Earth Syst. Sci.* **21**, 1741–1756 (2017).
46. Bouchard, B. et al. Impact of rain-on-snow events on snowpack structure and runoff under a boreal canopy. *EGUsphere* **2024**, 1–40 (2024).
47. McGurk, B. J. & Marsh, P. Flow-finger continuity in serial thick-sections in a melting Sierran snowpack. *IAHS Publ.-Ser. Proc. Rep.-Intern Assoc. Hydrol. Sci.* **228**, 81–88 (1995).
48. Rhoades, A. M. et al. Anticipating how rain-on-snow events will change through the 21st century: lessons from the 1997 new year's flood event. *Clim. Dyn.* **62**, 8615–8637 (2024).
49. Wang, R., Kumar, M. & Link, T. E. Potential trends in snowmelt-generated peak streamflows in a warming climate. *Geophys. Res. Lett.* **43**, 5052–5059 (2016).
50. Molini, A., Katul, G. G. & Porporato, A. Maximum discharge from snowmelt in a changing climate. *Geophys. Res. Lett.* **38**, https://doi.org/10.1029/2010GL046477 (2011).
51. Heggli, A., Hatchett, B., Schwartz, A., Bardsley, T. & Hand, E. Toward snowpack runoff decision support. *iScience* **25**, 104240 (2022).
52. Yazdandoost, F., Moradian, S., Izadi, A. & Aghakouchak, A. Evaluation of CMIP6 precipitation simulations across different climatic zones: uncertainty and model intercomparison. *Atmos. Res.* **250**, 105369 (2021).
53. Almazroui, M. et al. Projected changes in temperature and precipitation over the United States, Central America, and the Caribbean in CMIP6 GCMs. *Earth Syst. Environ.* **5**, 1–24 (2021).
54. Kharin, V. V., Zwiers, F. W., Zhang, X. & Wehner, M. Changes in temperature and precipitation extremes in the CMIP5 ensemble. *Clim. Change* **119**, 345–357 (2013).
55. Chan, S. C., Kendon, E. J., Roberts, N. M., Fowler, H. J. & Blenkinsop, S. Downturn in scaling of UK extreme rainfall with temperature for future hottest days. *Nat. Geosci.* **9**, 24–28 (2016).
56. Fowler, H. J. et al. Anthropogenic intensification of short-duration rainfall extremes. *Nat. Rev. Earth Environ.* **2**, 107–122 (2021).
57. Zhang, X., Zwiers, F. W., Li, G., Wan, H. & Cannon, A. J. Complexity in estimating past and future extreme short-duration rainfall. *Nat. Geosci.* **10**, 255–259 (2017).
58. Bao, J., Sherwood, S. C., Alexander, L. V. & Evans, J. P. Future increases in extreme precipitation exceed observed scaling rates. *Nat. Clim. Change* **7**, 128–132 (2017).
59. Schroeer, K. & Kirchengast, G. Sensitivity of extreme precipitation to temperature: the variability of scaling factors from a regional to local perspective. *Clim. Dyn.* **50**, 3981–3994 (2018).
60. Berg, P., Moseley, C. & Haerter, J. O. Strong increase in convective precipitation in response to higher temperatures. *Nat. Geosci.* **6**, 181–185 (2013).
61. Westra, S. et al. Future changes to the intensity and frequency of short-duration extreme rainfall. *Rev. Geophys.* **52**, 522–555 (2014).
62. Eyring, V. et al. Overview of the coupled model intercomparison project phase 6 (CMIP6) experimental design and organization. *Geosci. Model Dev.* **9**, 1937–1958 (2016).
63. Sohrabi, M. M. et al. On the role of spatial resolution on snow estimates using a process-based snow model across a range of climatology and elevation. *Hydrol. Process.* **33**, 1260–1275 (2019).
64. Schmidli, J. *et al*. Statistical and dynamical downscaling of precipitation: an evaluation and comparison of scenarios for the European Alps. *J. Geophys. Res. Atmos.* **112**, https://doi.org/10.1029/2005JD007026 (2007).
65. Srivastava, A., Grotjahn, R. & Ullrich, P. A. Evaluation of historical CMIP6 model simulations of extreme precipitation over contiguous US regions. *Weather Clim. Extremes* **29**, 100268 (2020).
66. Kouki, K., Räisänen, P., Luojus, K., Luomaranta, A. & Riihelä, A. Evaluation of Northern Hemisphere snow water equivalent in CMIP6 models during 1982–2014. *Cryosphere* **16**, 1007–1030 (2022).
67. Abramowitz, G. et al. ESD reviews: model dependence in multi-model climate ensembles: weighting, sub-selection and out-of-sample testing. *Earth Syst. Dynam.* **10**, 91–105 (2019).
68. Maina, F. Z. & Kumar, S. V. Diverging Trends in Rain-On-Snow Over High Mountain Asia. *Earth's. Future* **11**, e2022EF003009 (2023).
69. Zhou, G., Zhang, D., Wan, J., Cui, M. & Zhang, S. Mapping reveals contrasting change patterns of rain-on-snow events in China during 2001–2018. *J. Hydrol.* **617**, 129089 (2023).
70. Mooney, P. A. & Li, L. Near future changes to rain-on-snow events in Norway. *Environ. Res. Lett.* **16**, 064039 (2021).
71. Beniston, M. & Stoffel, M. Rain-on-snow events, floods and climate change in the Alps: Events may increase with warming up to 4 °C and decrease thereafter. *Sci. Total Environ.* **571**, 228–236 (2016).
72. López-Moreno, J. I. et al. Changes in the frequency of global high mountain rain-on-snow events due to climate warming. *Environ. Res. Lett.* **16**, 094021 (2021).
73. Sindelar, H. Lessons from the 2022 Yellowstone Floods The Power of Documentary Film Interviews (2023).
74. White, A. B., Moore, B. J., Gottas, D. J. & Neiman, P. J. Winter storm conditions leading to excessive runoff above California's Oroville Dam

during January and February 2017. *Bull. Am. Meteorol. Soc.* **100**, 55–70 (2019).
75. Leung, L. R., Bader, D. C., Taylor, M. A. & McCoy, R. B. An introduction to the E3SM special collection: goals, science drivers, development, and analysis. *J. Adv. Model. Earth Syst.* **12**, e2019MS001821 (2020).
76. Golaz, J.-C. et al. The DOE E3SM coupled model version 1: overview and evaluation at standard resolution. *J. Adv. Model. Earth Syst.* **11**, 2089–2129 (2019).
77. Hao, D. et al. A parameterization of sub-grid topographical effects on solar radiation in the E3SM Land Model (version 1.0): implementation and evaluation over the Tibetan Plateau. *Geosci. Model Dev.* **14**, 6273–6289 (2021).
78. Hao, D. et al. Improving snow albedo modeling in the E3SM land model (version 2.0) and assessing its impacts on snow and surface fluxes over the Tibetan Plateau. *Geosci. Model Dev.* **16**, 75–94 (2023).
79. Li, L., Bisht, G., Hao, D. & Leung, L. Y. R. Global 1km land surface parameters for kilometer-scale earth system modeling. *Earth Syst. Sci. Data Discuss.* **2023**, 1–47 (2023).
80. Hao, D. et al. Evaluation of E3SM land model snow simulations over the western United States. *Cryosphere* **17**, 673–697 (2023).
81. Sun, N. et al. Regional snow parameters estimation for large-domain hydrological applications in the Western United States. *J. Geophys. Res. Atmos.* **124**, 5296–5313 (2019).
82. Fontrodona-Bach, A., Schaefli, B., Woods, R., Teuling, A. J. & Larsen, J. R. NH-SWE: Northern Hemisphere snow water equivalent dataset based on in situ snow depth time series. *Earth Syst. Sci. Data* **15**, 2577–2599 (2023).
83. Zeng, X., Broxton, P. & Dawson, N. Snowpack change from 1982 to 2016 over conterminous United States. *Geophys. Res. Lett.* **45**, 12,940–912,947 (2018).
84. Falcone, J. A. *GAGES-II: Geospatial Attributes of Gages for Evaluating Streamflow* (US Geological Survey, 2011).
85. Xia, Y. et al. Continental-scale water and energy flux analysis and validation for the North American Land Data Assimilation System project phase 2 (NLDAS-2): 1. Intercomparison and application of model products. *J. Geophys. Res. Atmos.* **117**, https://doi.org/10.1029/2011JD016048 (2012).
86. Livneh, B. et al. A spatially comprehensive, hydrometeorological data set for Mexico, the U.S., and Southern Canada 1950–2013. *Sci. Data* **2**, 150042 (2015).
87. Thornton, P. E., Running, S. W. & White, M. A. Generating surfaces of daily meteorological variables over large regions of complex terrain. *J. Hydrol.* **190**, 214–251 (1997).
88. Daly, C., Neilson, R. P. & Phillips, D. L. A statistical-topographic model for mapping climatological precipitation over mountainous terrain. *J. Appl. Meteorol. Climatol.* **33**, 140–158 (1994).
89. Bohn, T. J. et al. Global evaluation of MTCLIM and related algorithms for forcing of ecological and hydrological models. *Agric. For. Meteorol.* **176**, 38–49 (2013).
90. Marks, D., Winstral, A., Reba, M., Pomeroy, J. & Kumar, M. An evaluation of methods for determining during-storm precipitation phase and the rain/snow transition elevation at the surface in a mountain basin. *Adv. Water Resour.* **55**, 98–110 (2013).
91. Dai, A. Temperature and pressure dependence of the rain-snow phase transition over land and ocean. *Geophys. Res. Lett.* **35**, https://doi.org/10.1029/2008GL033295 (2008).
92. Jennings, K. S., Winchell, T. S., Livneh, B. & Molotch, N. P. Spatial variation of the rain–snow temperature threshold across the Northern Hemisphere. *Nat. Commun.* **9**, 1148 (2018).
93. Musselman, K. N., Molotch, N. P. & Margulis, S. A. Snowmelt response to simulated warming across a large elevation gradient, southern Sierra Nevada, California. *Cryosphere* **11**, 2847–2866 (2017).
94. Ban, Z. et al. Snowmelt-radiation feedback impact on Western U.S. streamflow. *Geophys. Res. Lett.* **50**, e2023GL105118 (2023).
95. Bonsoms, J., López-Moreno, J. I., Alonso-González, E., Deschamps-Berger, C. & Oliva, M. Rain-on-snow responses to warmer Pyrenees: a sensitivity analysis using a physically based snow hydrological model. *Nat. Hazards Earth Syst. Sci.* **24**, 245–264 (2024).
96. Alduchov, O. A. & Eskridge, R. E. Improved magnus form approximation of saturation vapor pressure. *J. Appl. Meteorol. Climatol.* **35**, 601–609 (1996).

Acknowledgements

This research was supported by the U.S. Department of Energy (DOE), Office of Science, Office of Biological and Environmental Research and Advanced Scientific Computing, Scientific Discovery through Advanced Computing (SciDAC) program. This research was conducted at Pacific Northwest National Laboratory (PNNL), which is operated for the U.S. DOE by Battelle Memorial Institute under contract DE-AC05-76RL01830. This research used computing resources from DOE BER Earth and Environmental Systems Modeling program's Compy cluster located at PNNL.

Author contributions

D.H. and G.B. designed research; D.H. performed research; D.H. analyzed data; D.H., G.B., D.X., M.K, and L.R.L. wrote the paper.

Competing interests

The authors declare no competing interests.

Additional information

Supplementary information The online version contains supplementary material available at https://doi.org/10.1038/s43247-025-02354-6.

Correspondence and requests for materials should be addressed to Dalei Hao.

Peer review information *Communications Earth & Environment* thanks Daniel Wright and Alan Rhoades for their contribution to the peer review of this work. Primary Handling Editor: Alireza Bahadori. A peer review file is available.